Supporting information

Synthesis

- Synthesis: MOF-808 nanocrystals (average size: 35 nm) and the $Fe^{III}(Sal_2trien)NO_3$ complex were prepared using previously published procedures.[1,2]

- Preparation of the MOF-808 films by spin-coating: 35 nm MOF-808 nanocrystals were first dispersed in ethanol at 30 mg/mL. The films were then prepared by deposition of 100 µL of the dispersion onto a transparent glass cover in rotation at 1000 rpm. Multiple depositions (3 or 5) were performed to obtain films that hold a certain degree of transparency as well as present suitable thickness to lead to an intense color after the insertion of the SCO complex.

- Encapsulation of the SCO complexes: To encapsulate the complex in a MOF-808 film, a 5 mL DCM solution containing 5 mg $Fe^{III}(Sal_2trien)NO_3$ complex was first prepared. The film was later placed face-up in the solution and stored at 5 °C overnight. Fresh DCM was used to remove excess SCO complexes after the loading process.

Experimental Methods

SEM-EDX: SEM images were recorded with FEI Magellan 400 scanning electron microscope. Si wafer were used as substrates to compensate for the electron accumulation during SEM measurements. atm % of Fe and Zr were evaluated based on the average of several measurements performed on different spots.

DLS measurements: Zeta potential and DLS size measurements of hydrodynamic radii were made on a Malvern Zetasizer Nano-ZS (Malvern Instruments).

Magnetic measurements: Magnetic susceptibility was recorded with a Quantum Design SQUID Magnetometer between 100 and 300 K at a sweep rate of 0.5 K/min under an applied field of 5 kOe. Samples of ca. 10 mg were enclosed in a diamagnetic sample holder. For the measurements with solvent in the pores, the powder was first put in contact with saturated vapor for a few hours before being quickly transferred to a closed hermetic sample holder. The data were normalized to get the magnetic susceptibility by mole of iron complex using the Zr/Fe atomic ratio obtained by EDX and knowing the molar weight of both the host MOF and the encapsulated complex. Note that due to the number of hypotheses involved during the data processing (diamagnetic correction, amount of complex loaded in the MOF, etc.), the final $\chi_M T$ product is obtained with a precision of ca. 0.3 $emu \cdot K \cdot mol^{-1}$).

Spin coating: MOF-808 NPs dispersed in ethanol were chosen for spin coating. The suspension was prepared from the moist product and its concentration was 30 mg/mL. The films were deposited on transparent glass covers at 1000 rpm. In each deposition, 100 µL of liquid was injected in order to guarantee a complete coverage of the substrate. Multiple depositions were

adopted to obtain films that hold a certain degree of transparency as well as present suitable thickness to lead to an intense color after the insertion of the SCO complex.

Sensing setup: The home-made sensing setup is composed of two main parts: the vapor generating section and the absorption measurement chamber. The vapor generating section employs a carrier gas (N_2 in our case), a mass flow controller (MFC) and a bubbler with precise temperature control. Regulation of the vapor concentration can be achieved by modifying the carrier flow or the temperature of the bubbler. The outlet of the bubbler is then connected to the inlet of the in-situ measurement chamber. The measurement chamber is embedded in a movable section of a Fluorolog spectrometer from Horiba equipped with a device to record UV-visible absorption spectra between 250 nm to 800 nm. It contains a photomultiplier, a piece of transparent glass and a screw lid for sealing coupled with an inlet and an outlet for the vapor flow. Once a film is placed in the chamber, its absorption spectrum can thus be recorded actively under the exposure of target analytes. The outlet is attached to a sink for the removal of generated vapor.

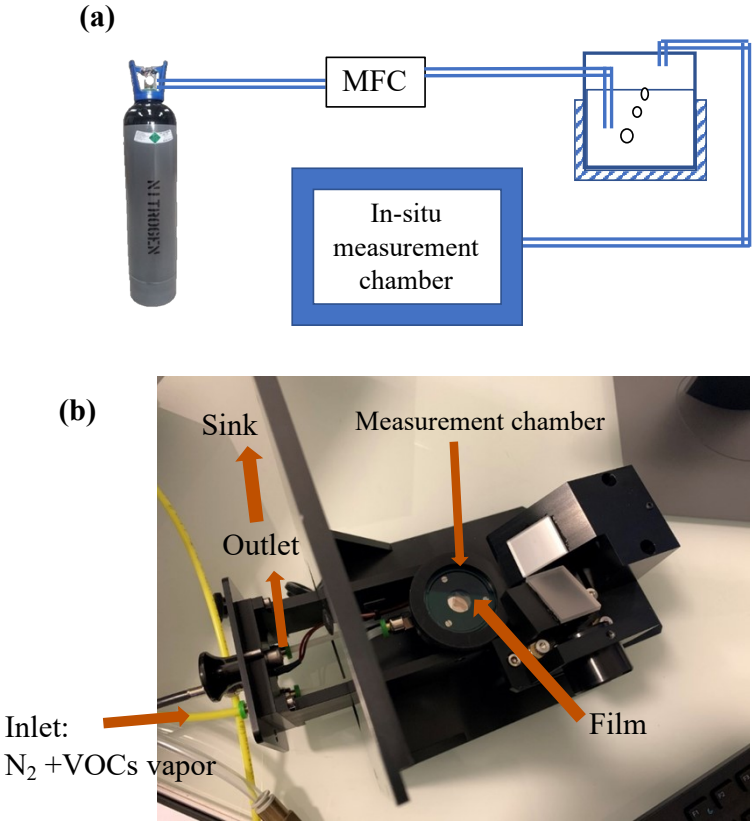

Figure S1. (a) Scheme of the vapor flow system. A nitrogen bottle is connected to a mass flow controller (MFC), coupled with a bubbler under temperature control. The vapor from the bubbler is then injected into the in-situ measurement chamber. (b) Photograph of the optical absorption measurement chamber.

Computational details

As in our previous simulation,[2] we adopted for the structure of MOF-808 the one obtained from its disordered crystal structure (space group Fd-3m)[3] by removing the O4 atom and the O3-H3A group from the CIF file. The packmol program[4] has been used to generate the initial configuration of the complex included in MOF808 in the presence of DMSO molecules. The subsequent simulations have been done with the CP2K program package[5] using the semi-empirical tight-binding GFN-xTB method.[6] During the simulations, the cell parameter was kept fixed to its experimental value of a = 35.1364 Å.

The well-tempered metadynamics (WT-MTD) simulation[7] has been performed on Ga(sal$_2$trien)NO$_3$⊂MOF-808 in the presence of 30 DMSO molecules and the technique of multiple walkers,[8] with N = 6 walkers. A time step of 1 fs is employed for the underlying Born-Oppenheimer molecular dynamics (BOMD) simulations performed in the *NVT* ensemble at a temperature of T = 320 K controlled by massive thermostating using the canonical sampling through velocity rescaling (CSVR) method.[9] The Cartesian coordinates of the Ga atom (x_{Ga}, y_{Ga}, z_{Ga}) were used as collective variables (CVs), and the difference ΔT between the simulation temperature T and the sampling temperature for the CVs was set to ΔT = 1500 K (T+ΔT = 1820 K). The starting points for the walkers were taken from an equilibrated BOMD run of 20 ps duration. The WT-MTD simulations were performed for *ca* 73 ps. Figure S11 shows the reconstructed FES. The snapshot from the walker trajectories closest to the most stable minimum was used as starting configuration for additional BOMD simulations, after having substituted Ga^{III} by Fe^{III} and optimized the resulting system in the LS and in the HS state.

For the BOMD study of LS and HS Fe(sal$_2$trien)NO$_3$⊂MOF-808 in the presence of 30 DMSO at T = 320 K, the simulations were done using a time step of 1 fs and controlling the temperature by massive thermostating, as for the WT-MTD simulation. The production LS and HS simulations were run for ca 43 ps and 42 ps, respectively. The analysis of the recorded LS and HS trajectories were done using the TRAVIS program.[10]

Additional data

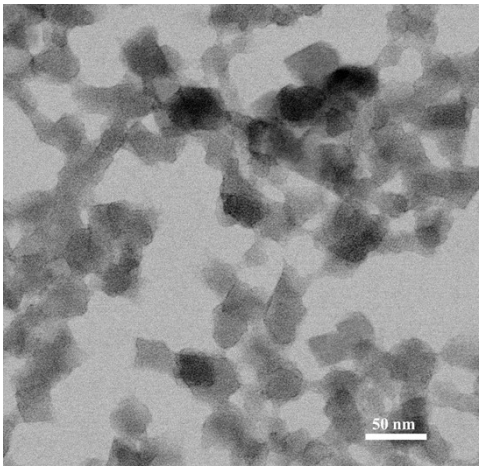

Figure S2. HRTEM image of 35 nm MOF-808.

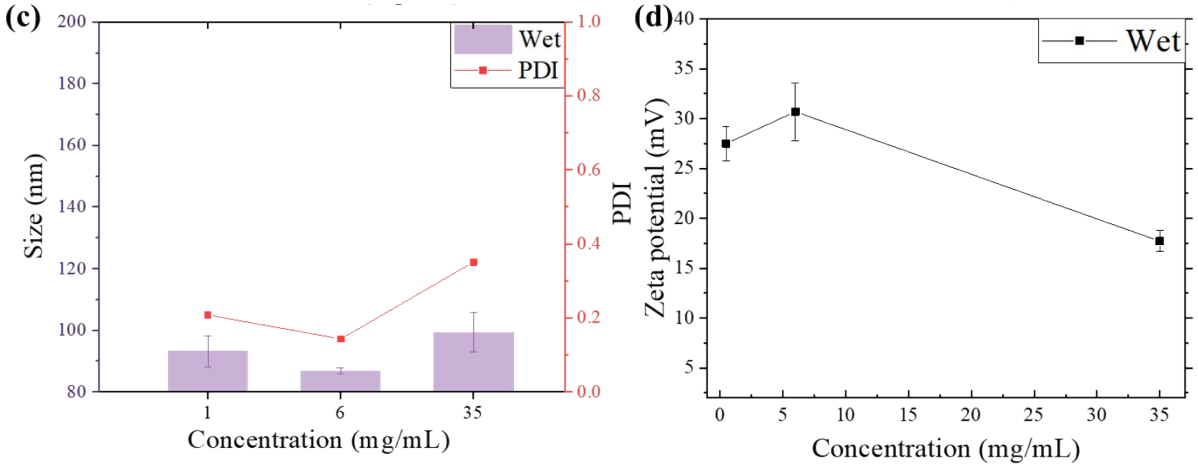

Figure S3. Size distribution of 35 nm MOF-808 NPs dispersed in EtOH (light purple) and PDI (red) at different concentrations. (d) Zeta potential of 35 nm MOF-808 NPs dispersed in EtOH at different concentrations.

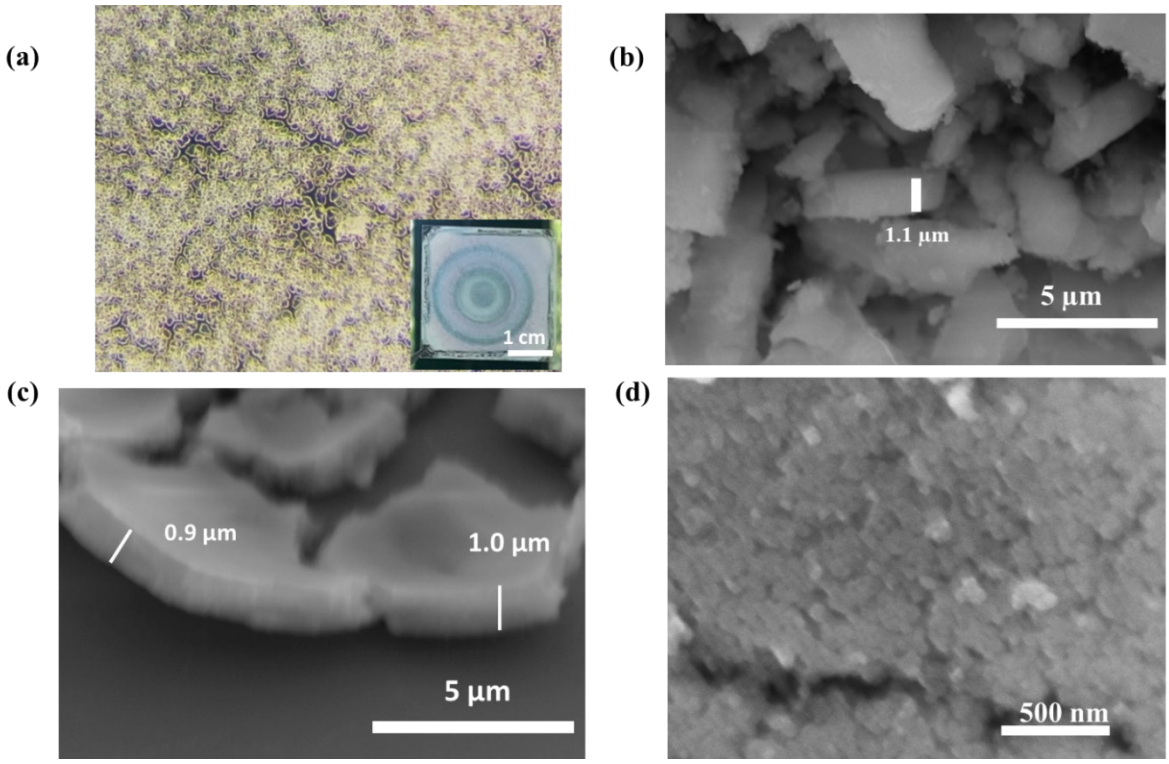

Figure S4. (a) Image of 3-layer deposition of MOF-808 films under a microscope. Inset: picture of the 3-layer MOF-808 films. (b) SEM images of film segments scrapped from the film on the glass cover. (c) SEM image of the cross-section of the film deposited on the Si wafer. The sample was placed on a 45°-titled measuring platform. A factor of cos(45°) was applied to the length measurement to correct the effect of the projection. (d) SEM images of the compact particles of the MOF-808 film.

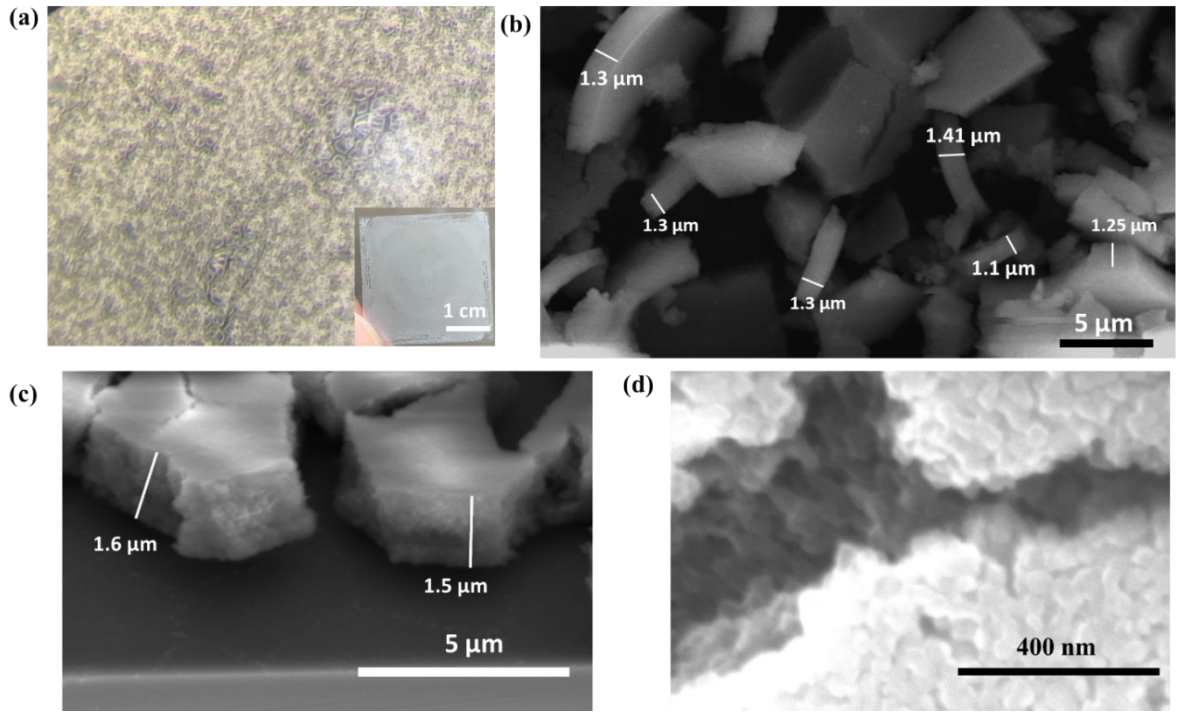

Figure S5. (a) Optical image of 5-layer deposition of MOF-808 NPs films under a microscope. Inset: picture of the 5-layer films. (b) SEM images of film segments scrapped from the film on the glass cover. (c) SEM image of the cross-section of the film deposited on Si wafer. A factor of cos(45°) was applied to the length measurement to correct the effect of the projection. (d) SEM images of the compact particles of the 5-layer deposition film.

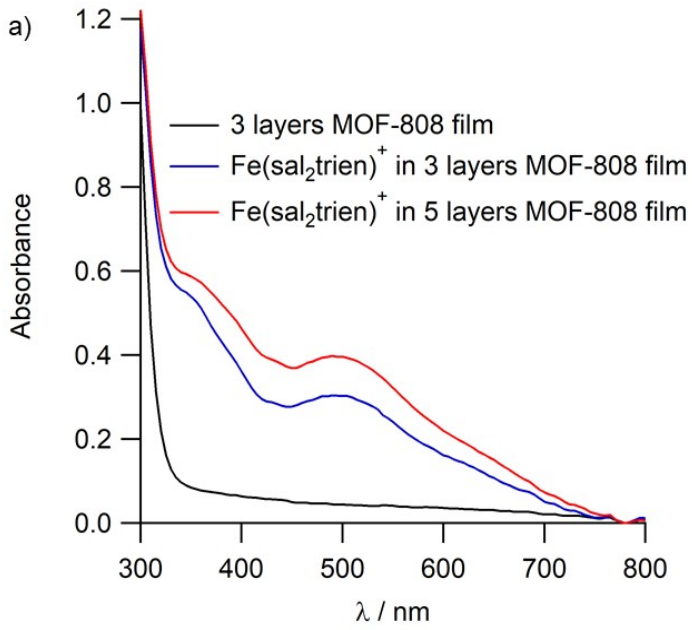

(b)	3 layers film	5 layers film
Thickness (µm)	1.0	1.5
Fe:Zr (atomic ratio)	0.23	0.17

Figure S6. (a) Optical absorption spectra of the pristine film and the films prepared with different parameters after loading. (b) Table of the thickness and the corresponding Fe: Zr ratio obtained by SEM-EDX analysis of different films.

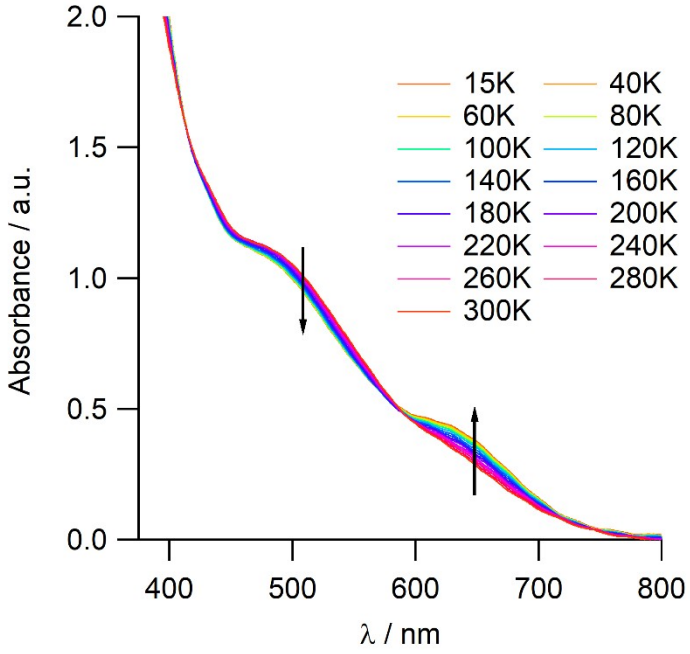

Figure S7. Evolution of the absorption spectrum of a 1.5 µm thick $Fe(Sal_2trien)NO_3$⊂MOF-808 film with the temperature between 15 and 300K (sweep rate of 1 K/min, arrows indicate the evolution of the spectrum upon cooling).

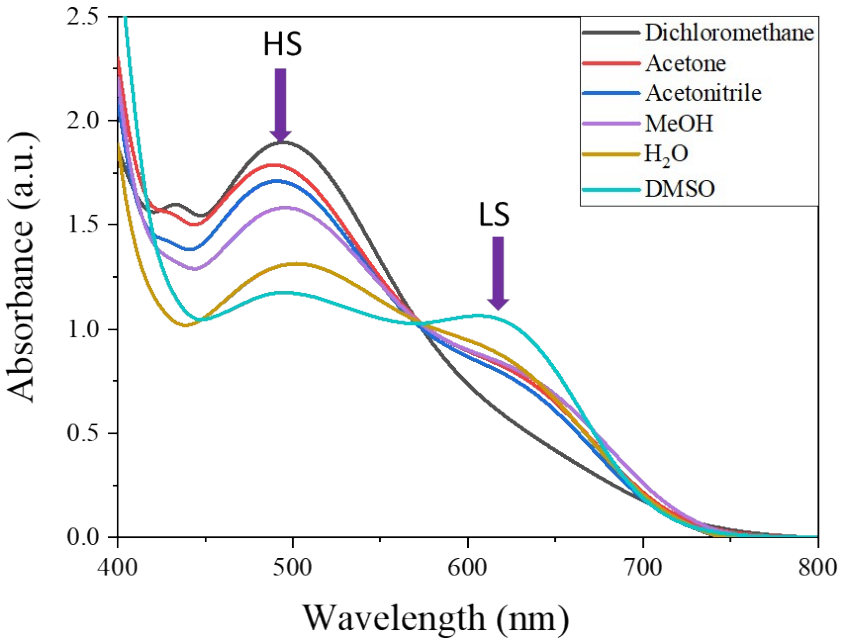

Figure S8. Optical absorption spectra of $Fe(Sal_2trien)NO_3$ in different solvents (at a concentration of 0.3 g/L).

The optical absorbance spectra of $Fe(Sal_2trien)NO_3$ dissolved in different solvents are depicted in Figure S8. Two predominant bands are observed at 500 nm and 620 nm, corresponding to LMCT transitions associated with the HS and LS states, respectively, in agreement with reported values. A solvatochromic behavior was observed at room temperature: the highest absorbance at 500 nm is observed in dichloromethane (DCM) and accordingly, the intensity of the 620 nm band is almost negligible. This suggests that the complex is mainly in the HS state in DCM. On the contrary, the complex in DMSO presents the most intense LS bands among others, which indicates a larger LS population than for other solvents. Intermediate HS and LS bands are observed for other solvents including acetone, acetonitrile, methanol, and water.

Evans NMR method was then applied to determine the magnetic susceptibility of the Fe^{III} complex in chosen solvents. For the measurements, a solution of the $Fe(Sal_2trien)NO_3$ complex in a given solvent was loaded into a NMR sample tube with a coaxial insert in order to measure the NMR signal of the solvent both with an without the complex. The frequency difference (Δf in Hz) between the two signals was used to determine the molar magnetic susceptibility of the complex in solution (see Figure S9 for an example of a NMR spectrum registered with this setup).

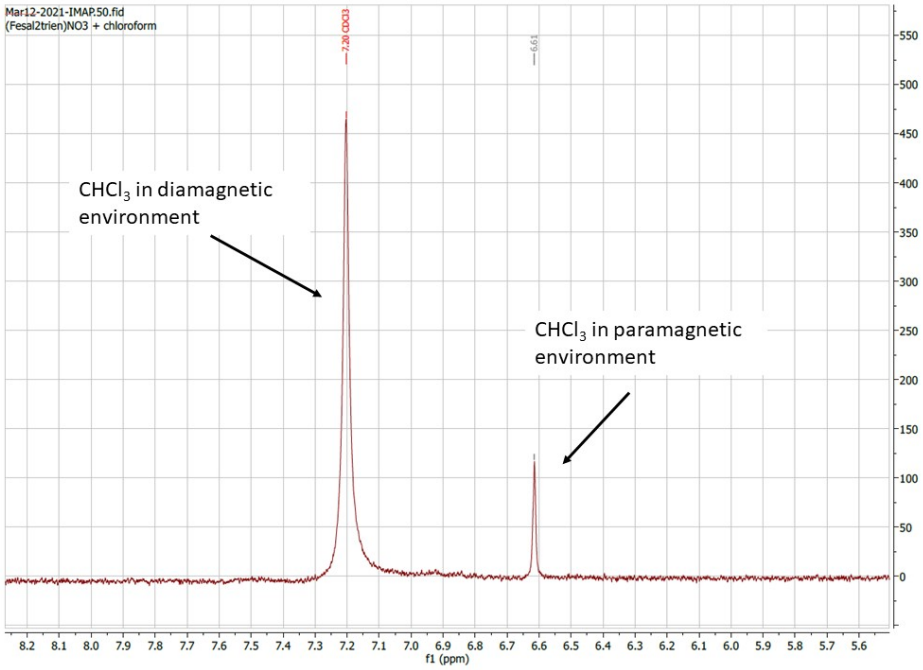

Figure S9. ^{1}H NMR spectra (300 MHz) of a solution of Fe(Sal$_2$trien)NO$_3$ in $CHCl_3$ (at a concentration of 5.35 g/L) and of $CHCl_3$ in a diamagnetic environment.

The results are summarized in
Table S1. Fe^{III} complexes with d^5 configuration in octahedral geometry have theoretical magnetic susceptibilities ranging from 5.9 μ_B (HS) to 1.7 μ_B (LS). The complex shows a susceptibility of 5.6 μ_B in chloroform, representing 93% of HS Fe^{III}. The value is 3.6 μ_B in DMSO, which corresponds to 52% HS. These results thus corroborate the optical absorbance spectra.

Table S1. Magnetic susceptibility of Fe(Sal$_2$trien)NO$_3$ in different solvents.

	Chloroform	**Methanol**	**DMSO**
Fe(Sal$_2$trien)NO$_3$	5.6 μ_B	4.4 μ_B	3.6 μ_B

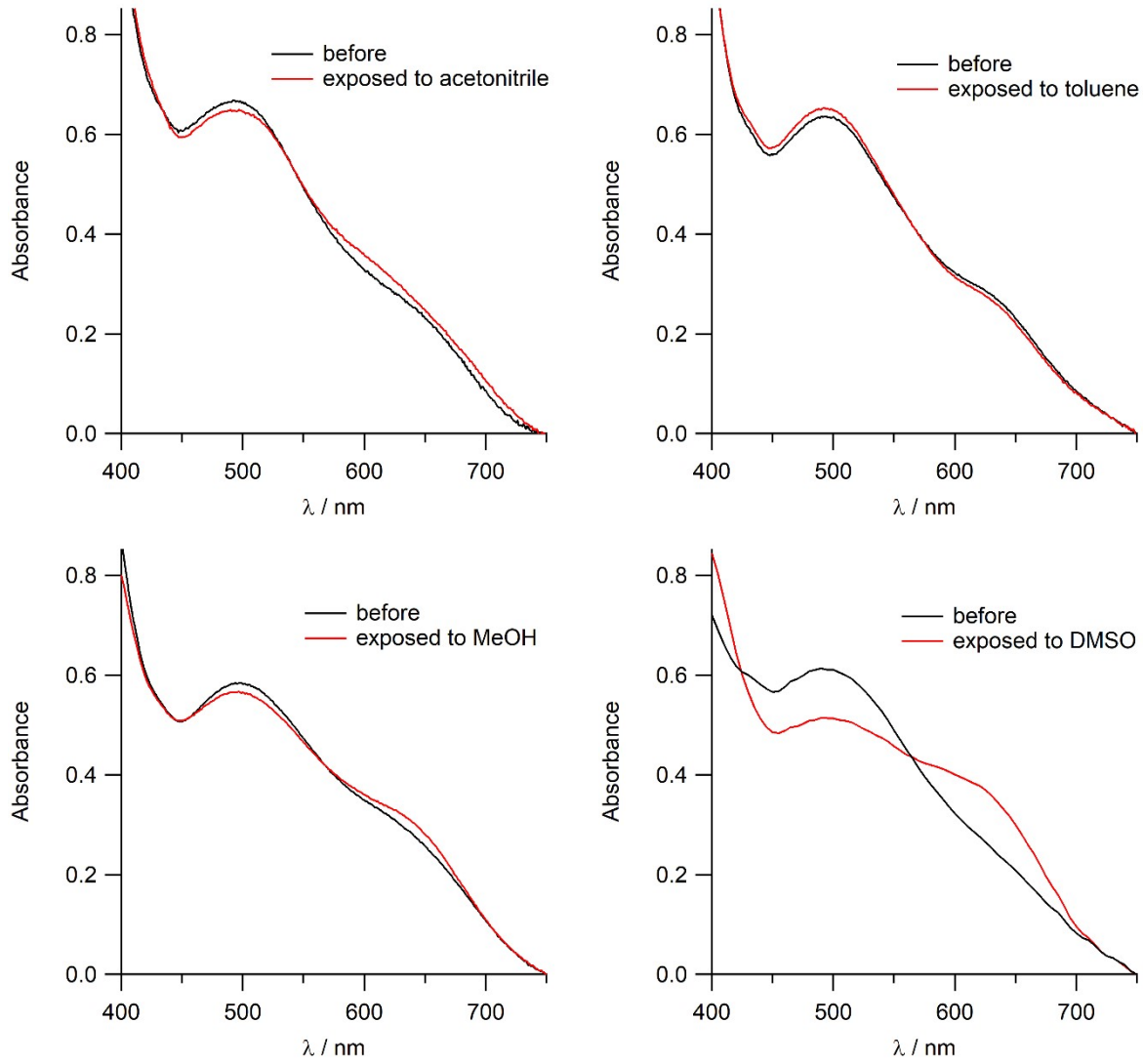

Figure S10. Absorption spectra of a Fe(Sal_2trien)NO_3⊂MOF-808 film before and after exposure to vapors of acetonitrile, toluene, methanol and DMSO.

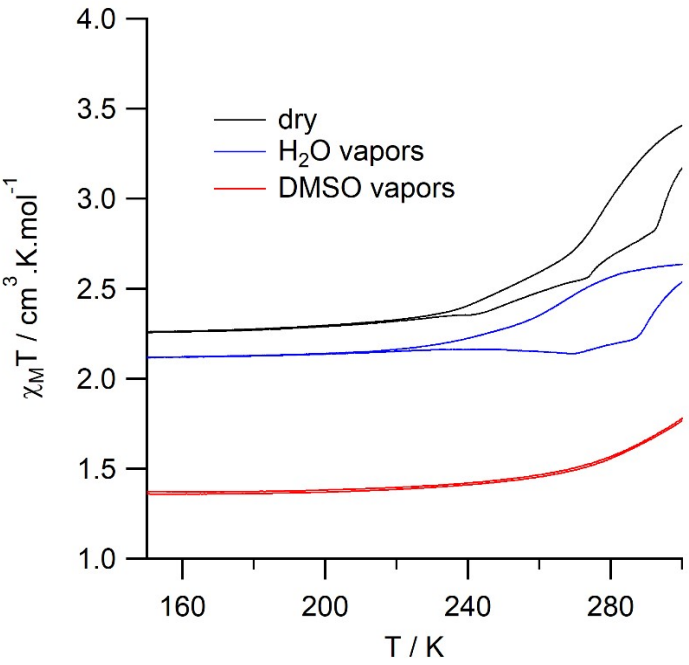

Figure S11. Evolution of the product of the molar magnetic susceptibility by the temperature as function of the temperature of an Fe(Sal_2trien)NO_3⊂MOF-808 powder dried before the measurement (black), saturated with water vapors before the measurement (blue) and saturated with DMSO vapors before the measurement (red).

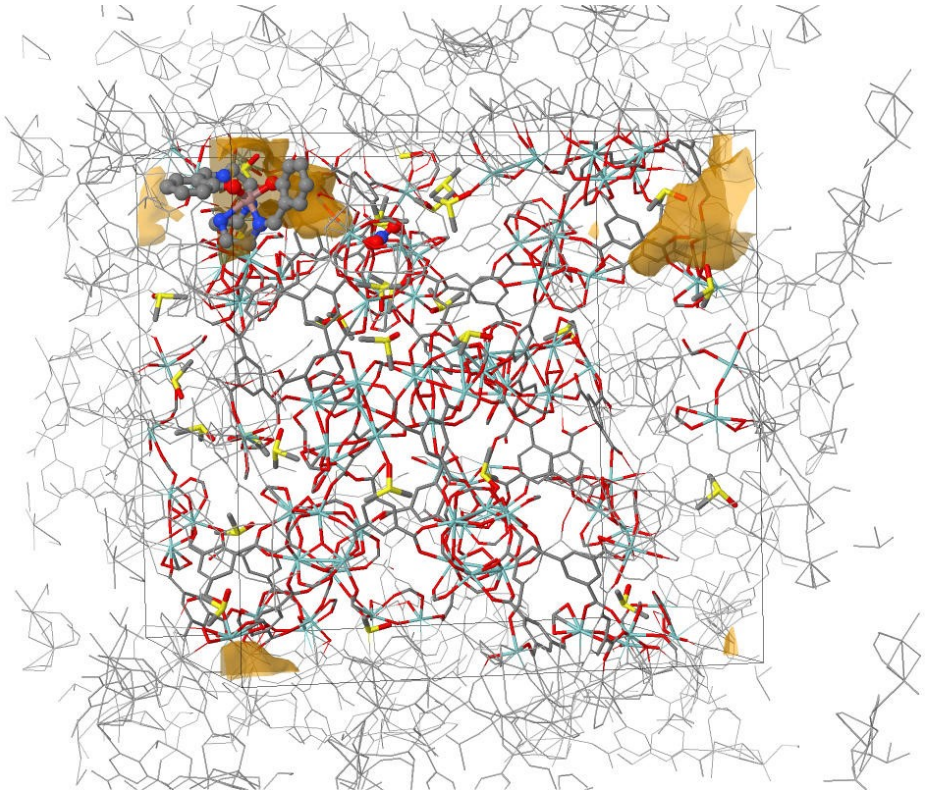

Figure S12. Free energy surface $F(T = 320$ K; x_{Ga}, y_{Ga}, $z_{Ga})$ calculated for the Ga(III) guest in the presence 30 molecules of DMSO (F = -20 mHa).

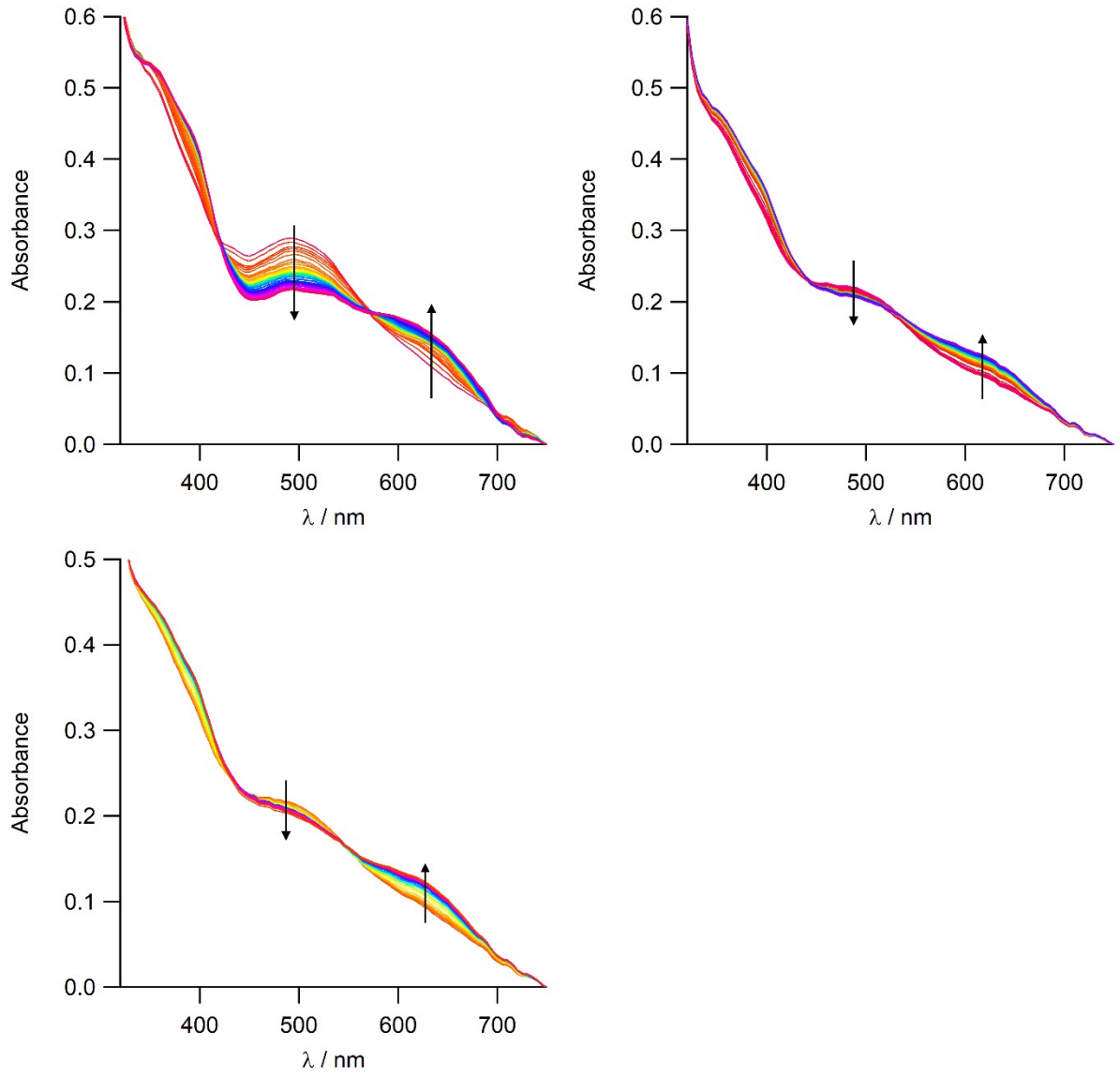

Figure S13. (top left) Evolution of the absorption spectrum of (top left) a 1.0 µm thick $Fe(Sal_2trien)NO_3 \subset$MOF-808 film exposed to 68 ppm_V DMSO vapors; (top right) a 1.5 µm thick $Fe(Sal_2trien)NO_3 \subset$MOF-808 film exposed to 15 ppm_V DMSO vapors; (bottom) a 1.5 µm thick $Fe(Sal_2trien)NO_3 \subset$MOF-808 film exposed to 15 ppm_V DMSO vapors in the presence of water vapor. In each experiment, the first spectrum is presented in red and the last one in blue.

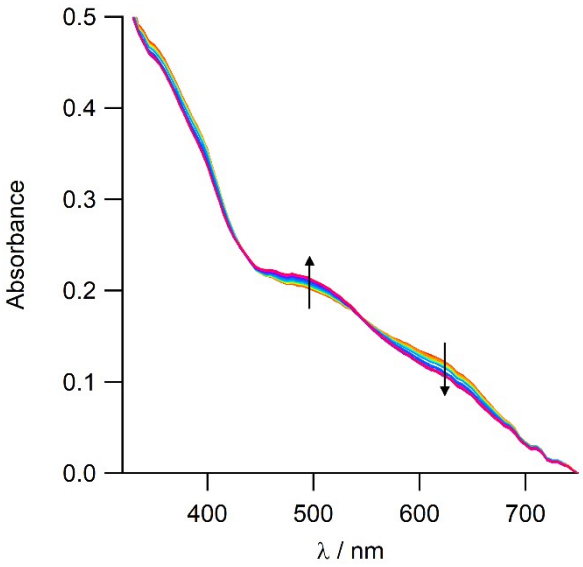

Figure S14. Evolution of the desorption spectrum of a 1.5 µm thick Fe(Sal_2trien)NO_3⊂MOF-808 film overnight after being exposed to 15 ppm_v DMSO. The first spectrum is presented in blue and the last one in red.

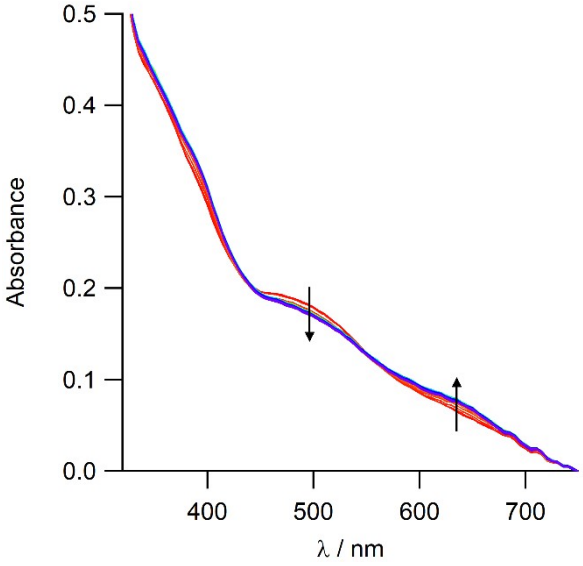

Figure S15. Evolution of the absorption spectrum of a 1.5 µm thick Fe(Sal_2trien)NO_3⊂MOF-808 film exposed to water vapors (> 1000 ppm_V). The first spectrum is presented in red and the last one in blue.

References

(1) Dai, S.; Simms, C.; Dovgaliuk, I.; Patriarche, G.; Tissot, A.; Parac-Vogt, T. N.; Serre, C. Monodispersed MOF-808 Nanocrystals Synthesized via a Scalable Room-Temperature Approach for Efficient Heterogeneous Peptide Bond Hydrolysis. *Chem. Mater.* **2021**, *33* (17), 7054–7066. https://doi.org/10.1021/acs.chemmater.1c02174.

(2) Shen, Y.; Woodburn, J.; Bouras, S.; Dai, S.; Dovgaliuk, I.; Grenèche, J.-M.; Patriarche, G.; Lawson Daku, L. M.; Serre, C.; Tissot, A. Room-Temperature Bistability in Spin Crossover-Loaded Metal–Organic Frameworks. *Chem. Mater.* **2023**, acs.chemmater.2c03426. https://doi.org/10.1021/acs.chemmater.2c03426.

(3) Trickett, C. A.; Osborn Popp, T. M.; Su, J.; Yan, C.; Weisberg, J.; Huq, A.; Urban, P.; Jiang, J.; Kalmutzki, M. J.; Liu, Q.; Baek, J.; Head-Gordon, M. P.; Somorjai, G. A.; Reimer, J. A.; Yaghi, O. M. Identification of the Strong Brønsted Acid Site in a Metal–Organic Framework Solid Acid Catalyst. *Nature Chem* **2019**, *11* (2), 170–176. https://doi.org/10.1038/s41557-018-0171-z.

(4) Martínez, L.; Andrade, R.; Birgin, E. G.; Martínez, J. M. P ACKMOL : A Package for Building Initial Configurations for Molecular Dynamics Simulations. *J Comput Chem* **2009**, *30* (13), 2157–2164. https://doi.org/10.1002/jcc.21224.

(5) Kühne, T. D.; Iannuzzi, M.; Del Ben, M.; Rybkin, V. V.; Seewald, P.; Stein, F.; Laino, T.; Khaliullin, R. Z.; Schütt, O.; Schiffmann, F.; Golze, D.; Wilhelm, J.; Chulkov, S.; Bani-Hashemian, M. H.; Weber, V.; Borštnik, U.; Taillefumier, M.; Jakobovits, A. S.; Lazzaro, A.; Pabst, H.; Müller, T.; Schade, R.; Guidon, M.; Andermatt, S.; Holmberg, N.; Schenter, G. K.; Hehn, A.; Bussy, A.; Belleflamme, F.; Tabacchi, G.; Glöß, A.; Lass, M.; Bethune, I.; Mundy, C. J.; Plessl, C.; Watkins, M.; VandeVondele, J.; Krack, M.; Hutter, J. CP2K: An Electronic Structure and Molecular Dynamics Software Package - Quickstep: Efficient and Accurate Electronic Structure Calculations. *J. Chem. Phys.* **2020**, *152* (19), 194103. https://doi.org/10.1063/5.0007045.

(6) Grimme, S.; Bannwarth, C.; Shushkov, P. A Robust and Accurate Tight-Binding Quantum Chemical Method for Structures, Vibrational Frequencies, and Noncovalent Interactions of Large Molecular Systems Parametrized for All Spd-Block Elements ($Z = 1–86$). *J. Chem. Theory Comput.* **2017**, *13* (5), 1989–2009. https://doi.org/10.1021/acs.jctc.7b00118.

(7) Barducci, A.; Bussi, G.; Parrinello, M. Well-Tempered Metadynamics: A Smoothly Converging and Tunable Free-Energy Method. *Phys. Rev. Lett.* **2008**, *100* (2), 020603. https://doi.org/10.1103/PhysRevLett.100.020603.

(8) Raiteri, P.; Laio, A.; Gervasio, F. L.; Micheletti, C.; Parrinello, M. Efficient Reconstruction of Complex Free Energy Landscapes by Multiple Walkers Metadynamics. *J. Phys. Chem. B* **2006**, *110* (8), 3533–3539. https://doi.org/10.1021/jp054359r.

(9) Bussi, G.; Donadio, D.; Parrinello, M. Canonical Sampling through Velocity Rescaling. *The Journal of Chemical Physics* **2007**, *126* (1), 014101. https://doi.org/10.1063/1.2408420.

(10) Brehm, M.; Thomas, M.; Gehrke, S.; Kirchner, B. TRAVIS—A Free Analyzer for Trajectories from Molecular Simulation. *The Journal of Chemical Physics* **2020**, *152* (16), 164105. https://doi.org/10.1063/5.0005078.